Power Electronic Systems
Laboratory

IEEE Transactions on Power Electronics, Vol. 28, No. 7, pp. 3591-3602, July 2013

Multiobjective Optimization of Ultraflat Magnetic Components With PCB-Integrated Core

C. Marxgut,
J. Mühlethaler,
F. Krismer,
J. W. Kolar

Eidgenössische Technische Hochschule Zürich
Swiss Federal Institute of Technology Zurich

Multiobjective Optimization of Ultraflat Magnetic Components With PCB-Integrated Core

Christoph Marxgut, *Student Member, IEEE*, Jonas Mühlethaler, *Student Member, IEEE*, Florian Krismer, *Member, IEEE*, and Johann W. Kolar, *Fellow, IEEE*

***Abstract*—In future applications, e.g., in ultra-flat OLED lamp drivers or flat screen power supplies, ultra-flat ac/dc and dc/dc converter systems are highly demanded. Therefore, the design and implementation of a printed circuit board (PCB)-integrated flyback transformer for a 1-mm-thin single-phase power factor correction rectifier is under investigation. In this paper, first an overview on several integration methods is given. It is shown that the PCB integration of magnetic cores allows us to achieve the required thickness of 1 mm and a high energy density. In a next step, the design and the realization of ultra-flat magnetic components with PCB-integrated cores are discussed in detail. The presented multi-objective design procedure determines the inductor and/or transformer setup optimal with respect to minimal losses and/or minimal footprint area; for this purpose, all required electrical, magnetic, and geometrical parameters of the magnetic component are considered in the design process. Furthermore, all specific implications entailed by the PCB-integrated core, e.g., the core setup, anisotropic core losses, the interleaving of windings, or an accurate reluctance model are treated. Finally, experimental results are used to verify the design procedure.**

***Index Terms*—Flyback transformer, PCB-integrated transformer, printed circuit board (PCB)-integrated inductor, power sheet, ultra-flat magnetics.**

I. Introduction

ULTRAFLAT power converters are increasingly needed for specific future applications, such as, e.g., ultra-flat OLED lamp drivers [1]–[4] or flat screen power supplies [5]. The respective power converters are single-phase power factor correction (PFC) rectifiers, which provide an output power between 20 and 200 W at a constant dc voltage (typically 10–20 V); the total converter height limit is typically 1–2 cm [6].

The Power Electronic Systems Laboratory at ETH Zurich aims to outperform this height requirement by a factor of 10 and to realize a PFC rectifier with a total height of only 1 mm. The related research project, entitled the *Power Sheet* [7], focuses on the analysis and the comprehension of the implications of the extremely low converter height on the PFC rectifier's efficiency and on the total required footprint area. Furthermore, the optimal converter design, with respect to efficiency or footprint area, is investigated.

Except for the magnetic components, all active converter components (e.g., power MOSFETs and control ICs) are available either in thin packages with thicknesses of less than 1 mm (i.e., thin SMD packaged semiconductor components) or as bare chips. Also, thin ceramic capacitors with thicknesses of less than 1 mm are commercially available [8], [9]. Printed circuit boards (PCB) with a total thickness of less than 1 mm can be realized and the aforementioned components (semiconductors, capacitors, and control circuits) can be embedded into the PCB [10]. Thus, the implementation of ultra-flat magnetic components is the main challenge that needs to be solved to keep the 1 mm height limit.

For realizing inductive components in an initial step, power SMD inductors could be considered; however, the total height of the flattest available power SMD inductors is over 3 mm [11]. As an alternative, planar magnetic cores and a multilayer PCB could be used to realize ultra-flat magnetic components [12]. Still, the realization of the required ultra-flat magnetic components is unfeasible, since the minimal total height of available planar cores is 5 mm (e.g., ELP 14/3.5/5 by [13]). In a different approach, flat magnetic components are implemented with PCB inductors consisting of spiral windings on several layers, which are covered with magnetic material [14]. Based on this integration method, a transformer for a 60 W power converter is realized in [15] (PCB thickness: 4 mm). The implemented core employs a ferrite polymer compound with a low relative permeability (typically $\mu_r = 10 \ldots 20$); therefore, a considerably large area is required in order to obtain the desired inductance value. Accordingly, this technique facilitates the realization of thin inductors; however, the energy density of the inductors is low due to the inherently large air gap length.

A reduced air gap length and an increased energy density are achieved if the core of the magnetic component is integrated into the PCB. In [16], the PCB integration of highly permeable magnetic materials ($Ni_{80}Fe_{20}$) is discussed; PCB-integrated core structures with a thickness of 1.3 mm have been built and are used as inductors for a 1.5 W buck converter. A comparison between closed core structures and air inductors is given, and it is shown that closed core assemblies provide the highest inductance and efficiency values per area. Since the employed magnetic cores are very thin (10–20 μm), a large area is required to avoid saturation for a given current and to achieve a required inductance value. Furthermore, in [16], the eddy current losses in the magnetic cores are large due to the selected arrangement of the winding and the core.

Manuscript received July 11, 2012; revised September 7, 2012 and October 15, 2012; accepted October 15, 2012. Date of current version December 24, 2012. Recommended for publication by Associate Editor C. R. Sullivan.

The authors are with the Power Electronic Systems Laboratory, Swiss Federal Institute of Technology Zurich, 8092 Zurich, Switzerland (e-mail: marxgut@lem.ee.ethz.ch; muehlethaler@lem.ee.ethz.ch; krismer@lem.ee.ethz.ch; kolar@lem.ee.ethz.ch).

Color versions of one or more of the figures in this paper are available online at http://ieeexplore.ieee.org.

Digital Object Identifier 10.1109/TPEL.2012.2226917

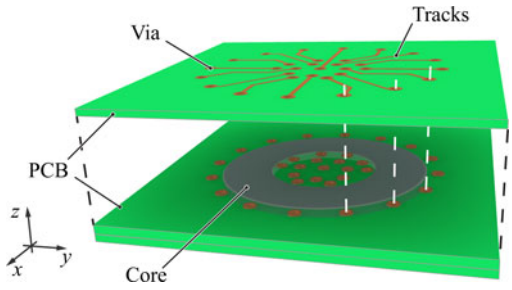

Fig. 1. PCB-integrated core; windings are realized with PCB tracks and vias.

TABLE I
SPECIFICATIONS OF THE *POWER SHEET* AT A THICKNESS OF 1 mm

$V_{\rm in}$	= 230 V	$T_{\rm amb}$	= 45 °C
$V_{\rm out}$	= 20 V	$f_{\rm S}$	= 160 kHz . . . 320 kHz
$P_{\rm out,tot}$	= 200 W	$N_{\rm mod}$	= 6
Galvanically isolated		$P_{\rm out,mod}$	= 33 W

O'Mathuna *et al.* [17] present a comprehensive review of integrated magnetics and describe several integration methods for inductors. However, the discussion focuses on very high frequency (HF) (1–100 MHz) point-of-load buck converters, e.g., for mobile phones, or multicore processors, with high current and low voltage capability. For an ac/dc rectifier where the isolation between the windings is crucial and the switching frequency is typically limited below 1 MHz, these integrated inductors are not feasible.

In [18], a ferrite core (Ferroxcube 3F3 [19]) is integrated into a PCB and applied to a buck converter (3.3 V/20 A). The inductance value is 1 μH and the integrated core has a thickness of 2 mm. Ferrite materials feature low core losses but it is very brittle and as the required magnetic cores are extremely thin (<1 mm), the production of ferrite cores is very difficult. Therefore, ferrites are not considered as an appropriate choice. Thus, amorphous and nanocrystalline soft magnetic materials remain, which enable a simpler manufacturing of ultrathin cores compared to ferrite cores. Zhang and Sanders [20] present a PCB-integrated transformer for a 200 W dc/dc converter employing an amorphous core material. Fig. 1 illustrates the construction of the magnetic component. However, the modeling of the transformer only accounts for eddy current losses and the geometry is restricted to toroidal cores.

This paper investigates the applicability of nanocrystalline and amorphous soft magnetic materials for the realization of ultra-flat magnetic components with almost arbitrary shape. This is illustrated on the example of the HF transformer of a single-phase flyback-type PFC rectifier with a total converter height of 1 mm and specifications according to Table I. The considered 200 W PFC rectifier, as presented in Fig. 2, is composed of six parallel flyback modules. The discussion in this paper refers to one of these six *Power Sheets* each rated with an output power of $P_{\rm out,mod} = 33$ W. The rectifier operates with zero-voltage switching, close to the boundary between continuous conduction mode and discontinuous conduction mode, to achieve low switching losses [21]. The system features only a single magnetic power component, i.e., the flyback transformer. A more

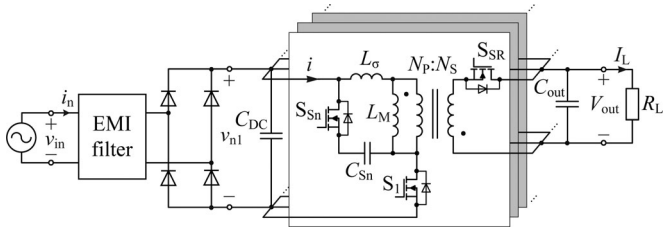

Fig. 2. Flyback-type single-phase PFC rectifier system, specified in Table I. The system is split up into six parallel interleaved modules ($N_{\rm mod} = 6$) in order to reduce the input and output capacitor currents. Each one of the parallel modules is referred as a *Power Sheet*.

common approach with input-side boost-type PFC rectifier and series-connected dc–dc converter shows a larger footprint area than the flyback-type approach, due to the two required magnetic components, i.e., the boost inductor and the HF transformer of the dc–dc converter.

The design of a PCB-integrated core differs from the design of conventionally shaped cores. Therefore, Section II discusses the specific requirements that need to be considered in the design, and Section III subsequently presents the optimization of ultra-flat magnetic components with respect to minimum total footprint area and/or minimum losses. The results of the multi-objective optimization are presented as η-α-Pareto Front, which shows the tradeoff between the area-related power density α (W/cm^2) and the efficiency η for a given magnetic core material.

Section IV presents measurement results obtained from a selected flyback transformer design being used in a dc–dc converter and in a single-phase PFC rectifier that are used to verify the theoretical considerations.

II. DESIGN CONSIDERATIONS FOR ULTRA-FLAT MAGNETIC COMPONENTS

The PCB integration of the core implies several specific properties and restrictions on the design of an inductor or transformer. This section discusses these implications required for the multi-objective design procedure presented in Section III and is divided into the following sections.

Section II-A summarizes the properties of the considered magnetic materials and discusses possible core constructions.

Section II-B emphasizes the importance of the isolation between the core tapes as otherwise the core losses increase vastly.

Section II-C focuses on the anisotropy of nanocrystalline and amorphous materials which results in increased losses in the easy magnetization direction.

Section II-D proposes a limit of the power loss per area in order to restrict the core temperature.

Section II-E presents an accurate reluctance model required for the inductance calculation of specific core geometries.

Section II-F details an interleaved winding arrangement for transformer applications.

A. Core Geometry and Materials

In order to integrate an inductor or a transformer into a PCB, the setup of the core has to be taken into consideration. There are

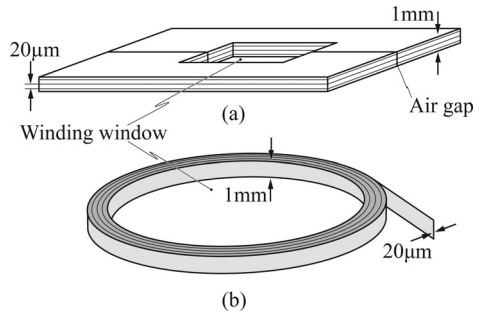

Fig. 3. Core configurations applicable to PCB-integrated transformers and inductors. (a) Two C-shaped core halves with stacked magnetic foils. (b) Toroidal core with a wound magnetic foil. In the latter setup (b), an air gap can only be inserted with considerable effort after embedding the core into the PCB.

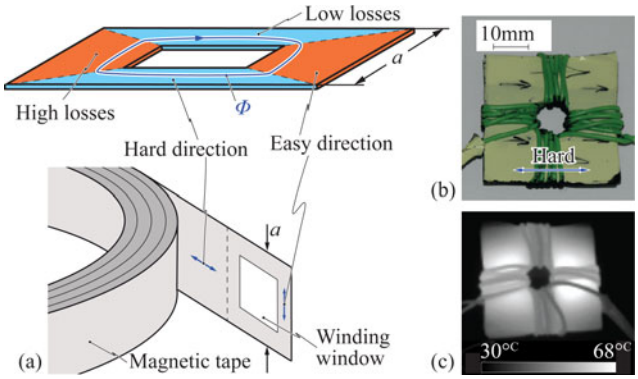

Fig. 4. (a) Magnetic sheets are cut out of a long band of magnetic foil. (b) Square inductor with a magnetic core formed by stacking ten sheets (VC6155F by VAC [23]) is shown. (c) Temperature rise in the easy direction is much higher compared to the hard direction ($f_S = 100$ kHz, $\Delta B = 1.5$ T, $P_{\rm loss} = 2.2$ W).

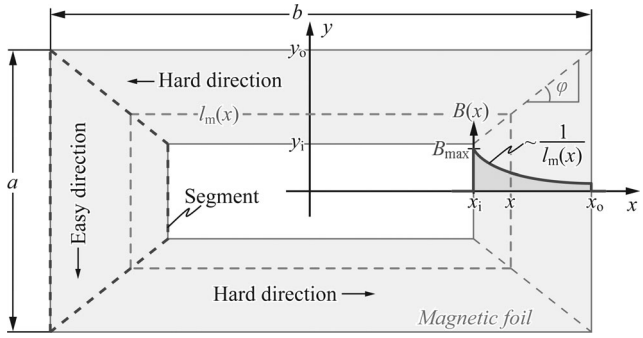

Fig. 5. Core geometry for the flux density calculation. To calculate the flux density and to determine the Steinmetz parameters for the easy direction, a rectangular-shaped core without air gap is considered.

basically two possible constructions for PCB-integrated magnetics employing nanocrystalline and amorphous materials. The core can either be composed of a stack of thin magnetic foils [cf., Fig. 3(a)] or it consists of a thin toroidally wound magnetic foil [cf., Fig. 3(b)]. However, an air gap, which offers the designer an additional degree of freedom, can only be easily realized for stacked assemblies as toroidally wound cores would fall apart. Only with a sophisticated core attachment inside the PCB an air gap can be implemented. The integration of the core into the PCB requires additional manufacturing effort compared to standard PCB production. However, this technology is already available (see, e.g., [22]) and thus not in the scope of this paper.

As mentioned Section I, nanocrystalline and amorphous materials are beneficial as ultrathin tapes of these materials are available that are suitable to realize the geometries in Fig. 3. These tapes feature a thickness of 20 μm or less and are applicable to HF applications. However, the width of the tapes, a, (cf., Fig. 4) is limited due to manufacturing reasons. This is a limitation in the design process of an integrated inductor and causes the cores to be either composed of several core legs or of a monolithic core with rather rectangular (cf., Fig. 5) than quadratic shape [cf., Fig. 4(b)] as otherwise the winding window [cf., Fig. 4(a)] would be too small to provide space for the windings.

Nanocrystalline materials are typically annealed in order to feature the specified magnetic properties. However, after the annealing process, these materials are very brittle, which makes a further mechanical treatment impossible. On the contrary, amorphous materials remain processable after being annealed. Amorphous materials are thus considered in this paper as they are beneficial for prototyping, whereas nanocrystalline cores need to be produced by the material manufacturer.

In this paper, the materials VITROVAC6155F by [23], termed in the following as VC6155F, and 2714A by [24] are investigated. Both materials are Cobald-based alloys, whereas VC6155F is field-annealed contrary to 2714A which is no-field annealed. Amorphous cores are typically employed for HF transformer and inductor applications and are available by various manufacturers [23]–[27].

B. Core Lamination

Lamination of magnetic cores is widely used for HF transformers and inductors as eddy currents and thus eddy current induced losses in the core material can be reduced. Therefore, the isolation between the magnetic foils is crucial to achieve low core losses in HF applications. Amorphous materials feature an inherent oxidation layer which reduces the conductance between two foils. However, measurement results show that the isolation provided by the oxide layer is insufficient. Two prototypes have been built up, where in the first one the magnetic foils are loosely embedded into the PCB, and in the second one, the core is tightly pressed into the PCB. It turns out that the losses increase with increasing pressure on the stack of foils (which increases the conductivity between the magnetic foils). The measurements have shown that the pressed setup generates three times higher losses than the loose realization ($\Delta B = 0.4$ T, $f_S = 100$ kHz: $P_{\rm loose} = 8.9$ W, $P_{\rm tight} = 29.25$ W).

To increase the resistance between the magnetic foils, either isolation tapes or isolation lacquer has to be employed. The addition of the isolation decreases the core fill factor $k_{\rm fe}$ that defines the ratio between the magnetically effective core cross-sectional area to the total cross section of the core. This has to be considered in the design procedure. Throughout this paper, the core foils are isolated using an isolation laquer in

order to obtain minimal core losses while keeping the core fill factor high.

C. Core Losses

An alternating magnetic flux in the core results in eddy current losses and hysteresis losses. A comparison between stacked and wound cores [cf., Fig. 3], however, shows that equal eddy current losses result for both configurations [28].

Hysteresis losses, however, show different behavior for both core configurations as nanocrystalline and amorphous materials are generally anisotropic, and there is an easy and a hard magnetizing direction of the foils. In toroidally wound cores, the flux is always in the tangential and therefore hard direction [cf., Fig. 4(a)]. In magnetic cores consisting of a stack of magnetic foils, the flux is forced to penetrate into the easy magnetizing direction as well. Fig. 4(a) shows that each sheet of the core is cut out of the magnetic band and the winding window is considered in the middle. The magnetic flux ϕ flows as indicated in Fig. 4(a) and higher losses in the easy magnetization direction have to be expected.

Fig. 4(b) shows a square prototype inductor which consists of a stack of ten VC6155F foils (each 20 μm thick) with a side length of 35 mm. Fig. 4(c) illustrates that an HF magnetic flux applied to the core results in different core losses for each direction; the temperature in the easy direction is higher compared to the hard direction.

It is, therefore, crucial that the increased losses in the easy direction are considered in the design of a PCB-integrated core. Otherwise, the core could be thermally damaged. Since core loss data for the hard direction are generally provided by manufacturers these parameters (k_h, α_h, and β_h) can easily be extracted. Thus, in order to be able to estimate the total core losses, the Steinmetz parameters for the easy direction remain to be determined. For it, a segmentation of the core according to Fig. 5 is assumed. The flux density in the core, $B(x)$, will decrease proportional to the inverse of the magnetic length $l_m(x)$ whereas the maximum flux density $B_{\max}$ is at the inner border of the core (x_i or y_i).

Referring to Ampère's law and considering Fig. 5, the ratio of the flux density at the outer and the inner edge is

$$\frac{B(x=x_i)}{B(x=x_o)} = \frac{l_m(x=x_o)}{l_m(x=x_i)} = \frac{4\cdot(x_o+y_o)}{4\cdot(x_i+y_i)}. \tag{1}$$

With

$$\begin{aligned} l_m(x) &= 4\cdot(x+y_i+(x-x_i)\cdot\tan\varphi) \\ &= 4\cdot\left(x+y_i+(x-x_i)\cdot\frac{y_o-y_i}{x_o-x_i}\right) \end{aligned}$$

the flux density at an arbitrary position x can be determined and is thus

$$B(x) = B_{\max}\cdot\frac{x_i+y_i}{x+y_i+(x-x_i)\cdot\frac{y_o-y_i}{x_o-x_i}}. \tag{2}$$

The core losses can be calculated with the Steinmetz equation that has to be integrated over either an easy or a hard direction segment. For the two segments in easy direction, the core losses

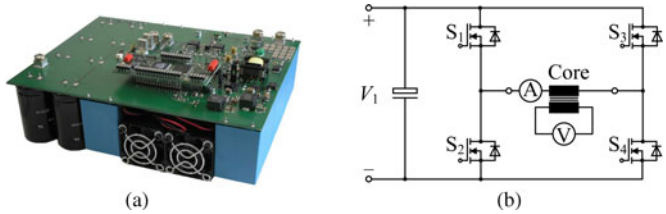

Fig. 6. (a) Picture and (b) circuit of the used core loss measurement system.

TABLE II
ESTIMATION OF THE LOSSES IN EASY MAGNETIZING DIRECTION BASED ON CORE LOSS MEASUREMENTS AND CALCULATIONS FOR THE CORE DEPICTED IN FIG. 4(b)

	$f_S = 200$ kHz		
ΔB	0.2 T	0.4 T	0.6 T
Calculated P_{hard} (cf. (3))	0.05 W	0.20 W	0.47 W
Measured P_{core} (cf. [29])	0.55 W	1.76 W	3.27 W
$\Rightarrow P_{\text{easy}}$ (cf. (4))	0.50 W	1.56 W	2.80 W

are thus

$$P_v = 2\,d_{\text{core}}k_{\text{fe}}\int_{x_i}^{x_o}\int_{-y_i-(x-x_i)\tan\varphi}^{y_i+(x-x_i)\tan\varphi} k_e\cdot f_S^{\alpha_e}\left(\frac{\Delta B(x)}{2}\right)^{\beta_e} dydx \tag{3}$$

with the core thickness d_{core} and the core filling factor k_{fe}. Equations similar to (2) and (3) can be determined for the hard magnetizing direction (i.e., $\Delta B(y)$) in the same way.

With this analytical background, the Steinmetz parameters related to the easy direction can be extracted from measurement results. For it, the core losses P_{core} of a given core under test (CUT) are measured at a certain operating point ($\Delta B, f_S$) using the core loss measurement system shown in Fig. 6 [29]. The core losses are obtained by applying an HF current to the core and by measuring the induced voltage on an auxiliary winding. The time integral of the induced voltage is proportional to the magnetic flux density in the core, and the applied current is proportional to the magnetic field. Thus, the core losses are extracted from the obtained hysteresis curve.

The core losses in hard direction, P_{hard}, can be calculated by applying the known Steinmetz parameters and the geometry of the CUT to (3). The difference between P_{core} and P_{hard} are the losses in the easy direction parts

$$P_{\text{easy}} = P_{\text{core}} - P_{\text{hard}}. \tag{4}$$

Table II presents the calculated and measured core losses for the CUT depicted in Fig. 4(b). In order to increase the accuracy of the Steinmetz parameter extraction, several square CUTs have been measured with different values of ΔB (0.2 T ... 1.8 T) and f_S (50 kHz ... 200 kHz). The obtained parameter sets ($P_{\text{easy}}, \Delta B, f_S$, and core geometry) are then applied to (3) which gives a set of equations. Finally, this overdetermined set of equations is solved for the Steinmetz parameters (k_e, α_e, and β_e) using a least-squares algorithm.

Fig. 7 presents a comparison between the amorphous materials VC6155F [23] and 2714A [24] based on the extracted Steinmetz parameters listed in Table III. It is shown that VC6155F has very low losses in the hard direction but high

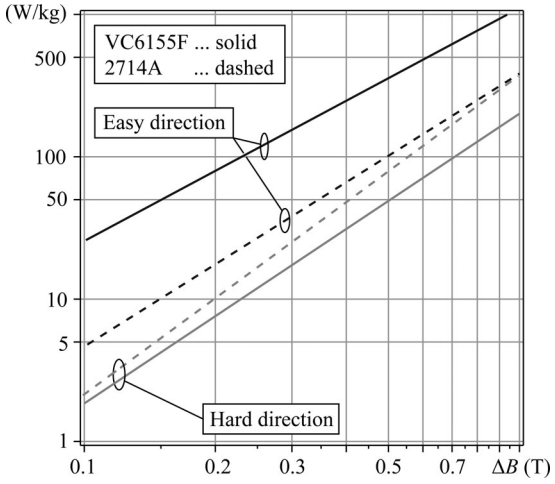

Fig. 7. Comparison of core losses between VC6155F according to [23] and 2714A according to [24] at $f_S = 100$ kHz. VC6155F features low core losses in the hard direction, whereas 2714A is better regarding the losses in the easy direction.

TABLE III
PARAMETERS OF MAGNETIC MATERIALS FOR INTEGRATED CORES

	a (mm)	B_{sat} (T)	ρ (kg/m^3)	Steinmetz parameters Hard (W/m^3)	Easy (W/m^3)
VC6155F [23]	35	1.0	7920	$k_{\mathrm{h}} = 0.0043$ $\alpha_{\mathrm{h}} = 1.84$ $\beta_{\mathrm{h}} = 2.04$	$k_{\mathrm{e}} = 0.074$ $\alpha_{\mathrm{e}} = 1.71$ $\beta_{\mathrm{e}} = 1.64$
2714A [24]	50	0.57	7590	$k_{\mathrm{h}} = 0.035$ $\alpha_{\mathrm{h}} = 1.71$ $\beta_{\mathrm{h}} = 1.91$	$k_{\mathrm{e}} = 2.99$ $\alpha_{\mathrm{e}} = 1.33$ $\beta_{\mathrm{e}} = 2.24$

losses in the easy direction. 2714A exhibits a more isotropic behavior.

D. Core Loss Per Area

For PCB-integrated magnetic components, thermal issues are important as the generated heat has to be transferred through the PCB to the ambient. In order to keep the core temperatures within reasonable limits, a maximum power loss per area, p_{loss}, is specified. Considering the area-related Steinmetz equation

$$p_{\mathrm{loss}} = k_{\mathrm{fe}} \cdot d_{\mathrm{core}} \cdot k(H_{\mathrm{dc}}) \cdot f_S^{\alpha} \cdot \left(\frac{\Delta B}{2}\right)^{\beta(H_{\mathrm{dc}})} \ (\mathrm{W/m^2}) \quad (5)$$

the maximum allowable flux density swing ΔB can be determined, which ensures the p_{loss} limitation. In (5), the impact of a dc offset H_{dc} can also be considered [30]. However, for the considered materials (VC6155F and 2714A), measurement results show almost no impact of the dc offset. With negligible impact of H_{dc} on p_{loss}, the closed-form solution for ΔB is

$$\Delta B = 2 \cdot \left(\frac{p_{\mathrm{loss}}}{k_{\mathrm{fe}} \cdot d_{\mathrm{core}} \cdot k \cdot f_S^{\alpha}}\right)^{1/\beta}. \quad (6)$$

Fig. 8 illustrates the calculation result of (6) for VC6155F in hard magnetizing direction; for a frequency of $f_{\mathrm{S}} = 160$ kHz and a power loss per area of $p_{\mathrm{loss}} = 0.33$ W/cm^2, the flux density swing ΔB must not exceed 920 mT. In the proposed design procedure, the flux density is thus limited to the minimum of

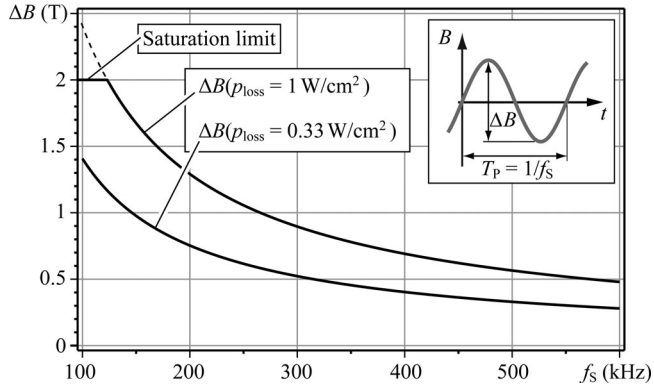

Fig. 8. Allowable ΔB for a specified power loss per area p_{loss} of a 1-mm-thick core without dc offset of B (Material: VC6155F, hard magnetizing direction). Considering a dc offset of B changes the saturation limit; however, the losses are almost offset independent for the considered material.

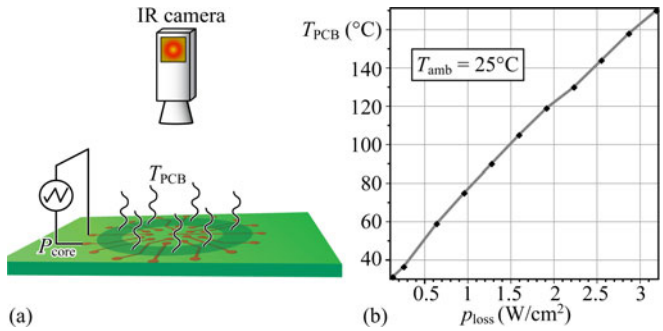

Fig. 9. (a) Setup of the thermal measurement for PCB-integrated cores. The measurement system presented in [30] has been applied to generate a core excitation and/or corresponding core losses. (b) Resulting temperatures for given power losses per area, p_{loss}.

either ΔB or the saturation flux density B_{sat}. Therefore, the geometry of the core has to be designed to keep the maximum flux density within this limit for a given flux value.

A reasonable value for the power loss per area, p_{loss}, is obtained using measurements, whereas the core losses are generated by proper excitation of the core and the temperature on the PCB is measured using an infrared camera. Fig. 9(a) shows the measurement setup and Fig. 9(b) presents the resulting temperatures for given power losses per area p_{loss}.

As the glass transition temperature for FR4 is 135 °C [31], the design procedure presented in Section III is performed with conservative value of $p_{\mathrm{loss}} = 0.3$ W/cm^2 which results in an expected temperature of $T_{\mathrm{PCB}} = 62$ °C at 40 °C ambient temperature, as specified in Table I.

E. Reluctance Model

The calculation of the desired inductance value of a PCB-integrated magnetic component requires the determination of the air gap length based on the known core reluctance. Depending on the shape and the size of the PCB-integrated core, the total core reluctance cannot be assumed to be lumped but rather consists of a mesh of reluctances. In order to be able to consider arbitrary shapes of PCB-integrated cores, Marxgut *et al.* [28] present an appropriate reluctance model used to determine the

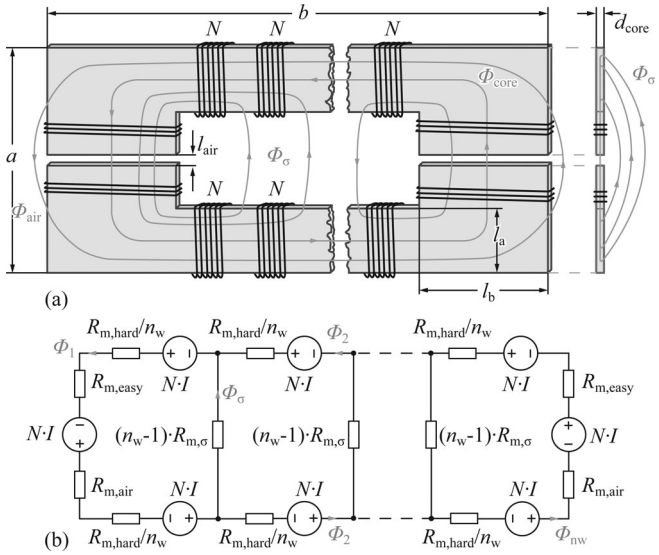

Fig. 10. (a) Setup of a PCB-integrated inductor; n_w winding packages, each with N turns, are placed around the core in order to later facilitate an interleaving with a secondary winding. (b) Reluctance model of the setup presented in (a). The reluctances $R_{m,\sigma}$ between the long magnetic rods have to be considered as they have considerable impact on the inductance for large ratios between core length and width, b/a.

air gap length and thus to adjust the inductance value. Whether a more complex reluctance model is required can be determined with a simulation showing the stray flux distribution.

Fig. 10(a) shows a typical two-part core configuration where an accurate reluctance model is crucial due to the comparably small reluctance $R_{m,\sigma}$ of the stray field path. Neglecting the winding window stray flux ϕ_σ would lead to a considerable deviation from the required inductance value. However, applying the reluctance model depicted in Fig. 10(b) and considering the 3-D fringing factor in the air gap (cf., [28] and [32]) results in an accurate air gap calculation and thus in the desired inductance value.

F. Interleaved Windings

In many transformer applications (e.g., flyback transformers), a low leakage inductance is crucial for a proper operation of the converter. In conventional transformers, the primary and secondary windings are, therefore, wound closely to each other and in many cases interleaved to maximize the coupling between the windings. In a PCB-integrated transformer, the windings are placed around the outlines of the core, which implies that the primary and secondary windings cannot be wound tightly together, and therefore, these transformers exhibit an inherently large leakage inductance.

In order to reduce the leakage inductance, an additional copper layer can be considered for the secondary winding which is placed on top of the primary winding. However, the extra copper layer comes at the expense of a thinner core as the overall thickness of the transformer is limited to 1 mm.

The coupling between the windings can be increased employing an interleaving of the winding arrangement [cf., Fig. 11(a)] along the outline of the core without compromising the thickness

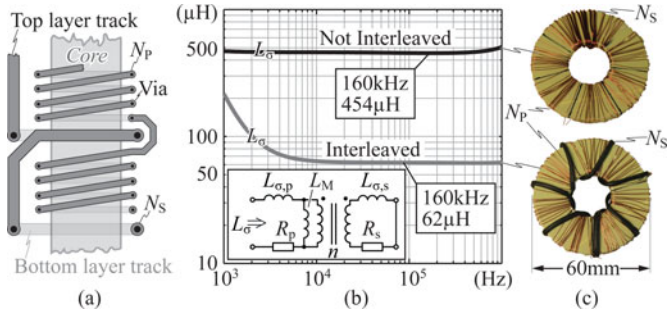

Fig. 11. (a) Interleaved winding arrangement. (b) Measurement result of the leakage inductance for an interleaved and a noninterleaved winding arrangement. (c) Prototypes used for the measurements: Ferrite N87, 1.5 mm thick, $N_P = 91$, and $N_S = 7$.

of the core. Applying the double-2-D FEM simulation method [33] enables the estimation of the leakage inductance and shows that the interleaved winding arrangement reduces the leakage inductance by a factor of 7.2 (noninterleaved: $L_\sigma = 377.6\ \mu$H and interleaved: $L_\sigma = 52.5\ \mu$H). In order to validate the simulations, measurements on a prototype core [cf., Fig. 11(c)] have been performed with both winding arrangements. Fig. 11(b) presents the results that show a considerable improvement with the interleaved configuration. The measurement of the interleaved configuration shows an inductance drop because for low frequencies $j\omega L_M > R_s + j\omega L_{\sigma,s}$ [cf. Fig. 11(b)], whereas for high frequencies, the leakage inductance determines the measurement result. The noninterleaved prototype shows the same characteristic but reaches its leakage inductance at lower frequencies due to the high value.

Due to the reduced L_σ, the prototype of the flyback transformer is realized employing the proposed interleaved winding arrangement.

III. Transformer Design Procedure

After the specific implications imposed by the ultrathin PCB-integrated core have been discussed in Section II, this section presents the design and the optimization of a flyback transformer (a two-winding inductor), employing a stacked core configuration which is integrated into the PCB [cf., Fig. 3(a)]. The proposed multi-objective design procedure that is depicted in Fig. 12(a) can easily be adapted for an inductor or for different core configurations [e.g., toroidal cores, cf., Fig. 3(b)]. Given all the input parameters listed in the flowchart, this step-by-step procedure leads to an optimal flyback transformer design with respect to a desired transformer efficiency $\eta_{\rm tr}$ or area-related power density $\alpha_{\rm tr}$

$$\eta_{\rm tr} = \frac{P_{\rm out}}{P_{\rm out} + P_{\rm loss}} \tag{7}$$

$$\alpha_{\rm tr} = \frac{P_{\rm out}}{A_{\rm tot}} \tag{8}$$

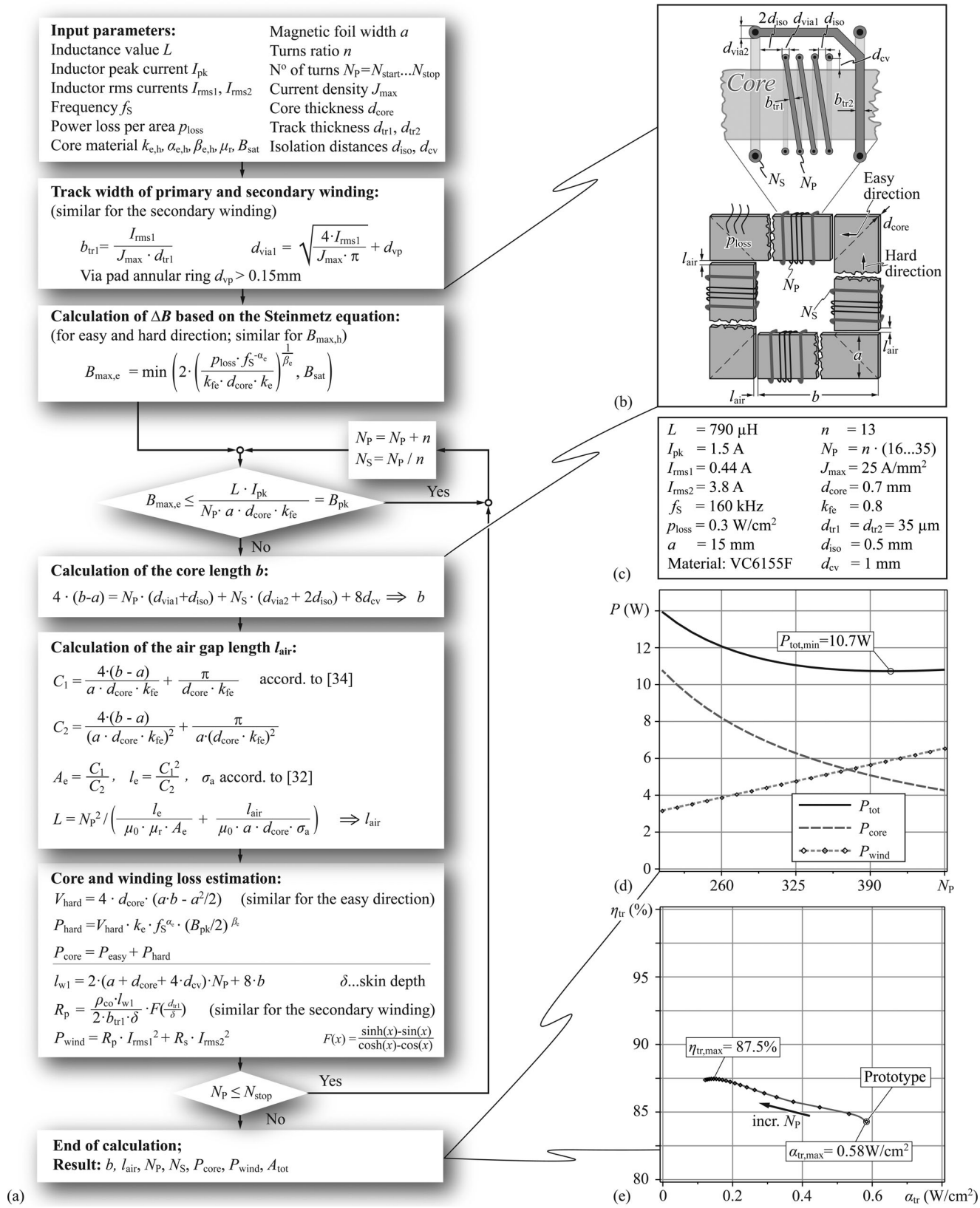

Fig. 12. (a) Block diagram of the design procedure of a flyback transformer with PCB-integrated core. (b) Illustration of the core and winding geometries. (c) Input parameter set. (d) Losses as a function of the number of turns for the parameters given in (c). (e) η-α-Pareto Front; a tradeoff between the efficiency η_{tr} and the area-related power density α_{tr} has to be found for a given inductor or transformer. The realized prototype is indicated in the figure.

whereas A_{tot} is the total required footprint area.[1] Each equation discussed in the following is given in Fig. 12(a).

The considered core geometry consists of four rectangular shaped core legs configured as indicated in Fig. 12(b) with an air gap l_{air} in each corner. The length b and the width a are identical for each core leg, so that the outline of the transformer is quadratic. An advantage of this core configuration is that, due to the four separate core legs, the flux is mostly directed toward the hard magnetizing direction [cf., Fig. 12(b)] and so less core losses are obtained compared to a core setup in which the easy magnetizing direction is more utilized [cf., Fig. 10(a)]. Besides, due to the air gaps in each corner of the core, the flux density can be assumed to be homogeneous in the core legs which has been validated using 3-D FEM simulations. A design procedure for an inhomogenous flux density distribution is presented in [28].

The core could also be rectangularly shaped to reduce the winding window; thus, the ratio between core length b and width a [cf., Fig. 10(a)] could be a further optimization parameter. However, for that purpose, a proper reluctance model as mentioned in the previous section is crucial. For brevity reasons, the presented optimization only considers square-shaped cores.

In a first step, the geometries of the windings are determined, which are depicted in Fig. 12(b); based on the track thickness $d_{\mathrm{tr1,2}}$ and the maximum allowable current density $J_{\max}$, the track widths $b_{\mathrm{tr1,2}}$ and the via diameters $d_{\mathrm{via1,2}}$ of both windings can be calculated (including the via pad annular ring d_{vp} which is typically > 0.15 mm).

In the next design step, the maximal allowable flux densities in the core, $B_{\max,e}$ and $B_{\max,h}$, are calculated for the easy and the hard magnetizing directions with respect to the maximum allowable power loss per area p_{loss} and the saturation flux density B_{sat} according to (6).[2] Then, the procedure queries whether the applied flux density exceeds $B_{\max,e,h}$ or not. If $B_{\mathrm{pk}} > B_{\max,e,h}$, the next iteration step starts with an increased number of turns N_P; otherwise, the procedure continues.

The perimeter of the winding window, $4 \cdot (b - a)$, has to be large enough to provide the space for all tracks and vias of primary and secondary windings including the isolation distances between the tracks, d_{iso}, and the distance between the core and the vias, d_{cv}. Solving this equation yields the required core leg length b.

As the core geometry is determined, the inductance value L can be adjusted by calculation of the required air gap length l_{air}. As mentioned in Section II-E, the fringing flux of the air gap must be considered in the air gap reluctance calculation. However, contrary to a setup composed of a monolithic or a two-part core [e.g., in Fig. 10(a)], in the chosen core configuration, the distance between two adjacent core legs is large so that the window stray reluctance $R_{m,\sigma}$ is negligible which has been confirmed using 3-D FEM simulations. Thus, a simple reluctance model composed of the core reluctance and the air gap reluctance can be applied.

[1]The optimization goal could easily be changed in order to consider only the area occupied by magnetics by defining a different area in (8).

[2]Since the core losses of the considered material are independent of a dc offset, $B_{\max,e/h} = \Delta B$. For other materials, the average current would also be an input parameter of the design procedure.

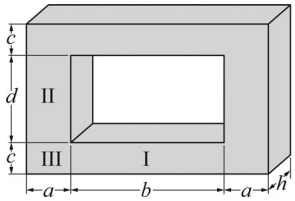

	l_i	A_i
I	b	$c \cdot h$
II	d	$a \cdot h$
III	$\frac{\pi}{4} \cdot (a+c)$	$\frac{h}{2} \cdot (a+c)$

$C_1 = \sum \frac{l_i}{A_i}$ $\quad C_2 = \sum \frac{l_i}{A_i^2}$

Fig. 13. Segmentation and corresponding equations of a rectangular core [34].

According to [34], an accurate reluctance model of a rectangular-shaped core can be obtained by considering the segmentation in Fig. 13. The coefficients C_1 and C_2 (cf., Fig. 13) are used to calculate the effective magnetic length l_e and the cross-sectional area A_e that define the reluctance of the core. The sum of core reluctance and air gap reluctance determines the inductance value L, and thus, the air gap length l_{air} can be calculated.

With all core and winding parameters being known, the core and winding losses can be determined. The core losses are evaluated using the Steinmetz equation applied to the easy and the hard magnetizing directions [cf., Fig. 12(b)]. The winding loss calculation based on only the dc resistance would yield an underestimation of the winding resistance R_W

$$R_W = R_p + n^2 \, R_s \tag{9}$$

by 34 % (calculated $R_W = 12.4\ \Omega$, measured $R_W = 18.9\ \Omega$ at $f_S = 160$ kHz [as will be shown in Section IV)]. In order to consider eddy-current-induced winding losses, the 1-D model presented in [35] and [36] is applied which results in a calculated value of $R_W = 15.5\ \Omega$. Still, compared to the measurement the calculation is lower by 18%. To further consider proximity effect caused losses, either sophisticated calculation methods [34], [37] or FEM simulations are required.

The design procedure is iterated over a specified range of $N_P = N_{\mathrm{start}} \ldots N_{\mathrm{stop}}$ with a step size of n which allows for integer values of N_S. Fig. 12(d) shows the core losses P_{core} and the winding losses P_{wind} as a function of N_P based on the parameters given in Fig. 12(c); minimal losses of $P_{\mathrm{tot,min}} = 10.7$ W are obtained for $N_P = 403$ and $N_S = 31$. Fig. 12(e) depicts a η-α-Pareto Front which shows that a compromise between the transformer efficiency η_{tr} and the area-related power density α_{tr} has to be found. The maximal power density for the considered design is $\alpha_{\mathrm{tr,max}} = 0.58$ W/cm^2 and the maximal efficiency of the transformer is $\eta_{\mathrm{tr,max}} = 87.5\%$. The power density α_{tr} considers the total required area; however, the winding window can also be utilized to place components which would increase the compactness of the converter system.

In the presented design procedure, the width of the magnetic foil, a, is chosen to be 15 mm due to the availability of the material. However, a is also a free design parameter that can be optimized. Fig. 14 shows the Pareto Front of VC6155F and 2714A for several values of $a = 0.5 \ldots 26$ mm (with a step size of $\Delta a = 0.5$ mm) and of $N_P = 13 \ldots 455$ (with a step size of $n = 13$).

As can be seen, VC6155F allows for higher efficiencies compared to 2714A. This is because in the chosen core configuration,

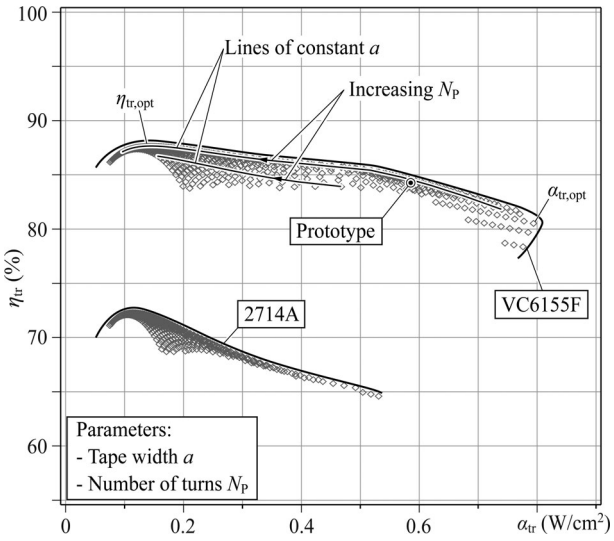

Fig. 14. Pareto Front for several values of N_P and a for the materials VC6155F and 2714A. The maximum efficiency achievable is $\eta_{\mathrm{tr,opt}} = 87.7\%$ ($a = 21.5$ mm, $N_P = 325$) and the maximum power density is $\alpha_{\mathrm{tr,opt}} = 0.79$ W/cm^2 ($a = 20.5$ mm, $N_P = 130$). The realized prototype is indicated in the figure.

the easy direction, which causes high losses in VC6155F, is barely utilized. Furthermore, the saturation flux density of 2714A is lower compared to VC6155F [cf., Table III] that explains the lower achievable power density of 2714A. However, for other core configurations and specifications, 2714A might be the material of choice.

Fig. 14 shows that α_{tr} increases with decreasing N_P for constant values of a due to the reduced area requirement of the winding. At $\alpha_{\mathrm{tr,opt}} = 0.79$ W/cm^2, the maximal power density is reached ($a = 20.5$ mm and $N_P = 130$) and a further decrease of N_P at constant a is not possible due to the limitation of the maximal flux density in the core. N_P can only be further decreased when a is increased (which increases the core cross section). This required increase of a is proportionally higher than the achieved reduction of the winding window, and thus, the total required footprint area increases. Consequently, a further power density increase is not possible anymore.

Starting from $\alpha_{\mathrm{tr,opt}}$, an increase of N_P and/or an increase of a decreases the flux density in the core which results in lower core losses. Thus, for increasing N_P and/or increasing a, the Pareto Front shows higher efficiencies at the expense of a lower α_{tr}. The decrease of core losses, however, is compromised by an increase of winding losses as the track lengths increase. Thus, the efficiency reaches a maximum where the decrease of core losses is equal to the increase of winding losses. The maximal efficiency is $\eta_{\mathrm{tr,opt}} = 87.7\%$ at $a = 21.5$ mm and $N_P = 325$. A further increase of N_P or a results in a lower efficiency as the increase of winding losses exceeds the decrease of core losses.

IV. Experimental Results

In order to verify the presented design procedure, a prototype of a flyback transformer for the PFC rectifier specified in Table I has been built up. For the flyback converter, a compact

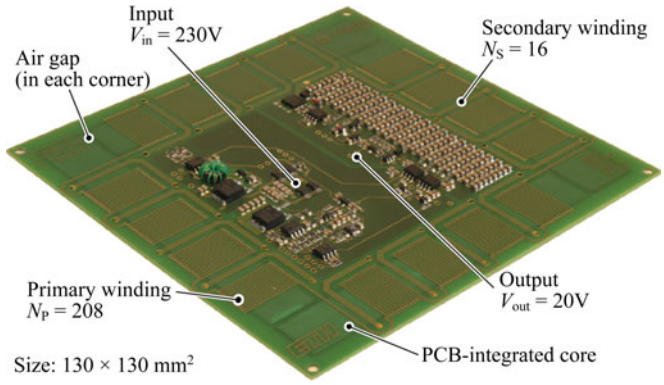

Fig. 15. Prototype of the flyback-type single-phase PFC rectifier with PCB-integrated transformer. Due to the large winding window, all components of the converter can be placed in the flyback transformer window area.

TABLE IV
Resulting Parameters of the Design Procedure for the Realized PCB-Integrated Flyback Transformer Rated With $P_{\mathrm{out}} = 76$ W

$a = c$	=	15 mm	P_{core}	=	10.8 W
$b = d$	=	100 mm	P_{wind}	=	3.2 W
l_{air}	=	0.8 mm	η_{tr}	=	84.3 %
d_{core}	=	0.7 mm	α_{tr}	=	0.58 W/cm^2
k_{fe}	=	0.8	A_{tot}	=	139 cm^2
N_{P}	=	208	B_{pk}	=	0.7 T
N_{S}	=	16			

transformer design has been chosen, as indicated in Fig. 12(e). Fig. 15 depicts the *Power Sheet* with PCB-integrated flyback transformer. The respective parameters are listed in Table IV. The prototype is realized with conventional SMD chips in order to simplify manufacturing and measurements. In a further step, these components can also be embedded in the PCB.

Fig. 16(a) presents measurement results of the primary inductance that matches well with the desired value (calculated: 790 μH, measured: $L_P = 772$ μH at 100 Hz). At the switching frequency of $f_S = 160$ kHz, the inductance decreases to $L_P = 741$ μH. Although primary and secondary windings are interleaved, the large spatial dimension of the transformer induces a rather high leakage inductance of $L_\sigma = 140$ μH which is in good agreement with simulation results. Due to the high L_σ, an active snubber is employed in the flyback converter which recycles the energy stored in the leakage inductance [38]. As alternatives, in [39] and [40], the authors present topologies in which the leakage inductance could be beneficially utilized. In Fig. 16(a), L_σ drops between 200 Hz and 10 kHz because for low frequencies the parallel connection of L_M with $L_{\sigma,s}$ and R_s is determined by L_M as its impedance is lower than $R_s + j\omega L_{\sigma,s}$. With increasing frequency, the impedance of L_M increases and the parallel connection is determined by $L_{\sigma,s}$.

The primary winding capacitance is 25 pF and the interwinding capacitance is 106 pF. The resulting resonance frequency is 1.1 MHz that is sufficient for the operation of the converter.

Fig. 16(b) shows the winding resistance R_W [cf., (9)] over the frequency. As already mentioned, the calculation underestimates the measurement by 18% (calculated $R_W = 15.5\ \Omega$, measured $R_W = 18.9\ \Omega$). Notice that at low frequencies, only the

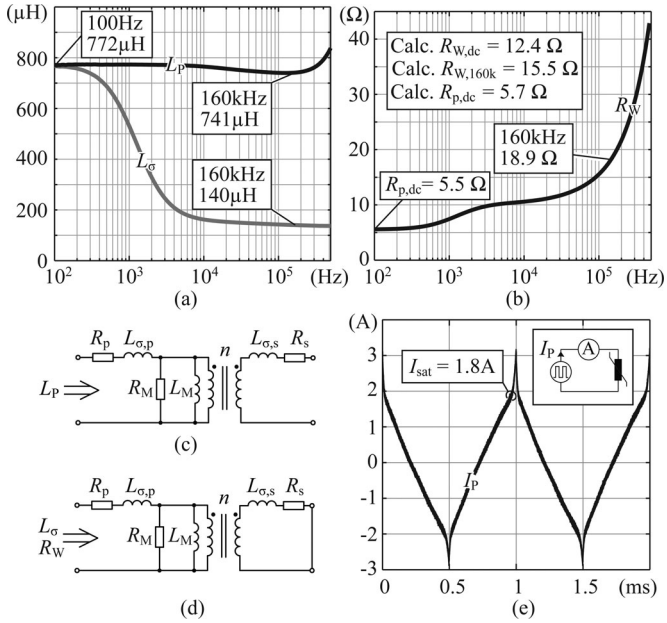

Fig. 16. (a) Total inductance L_P and leakage inductance L_σ over the frequency. (b) Total winding resistance $R_W = R_p + n^2 \cdot R_s$ referred to the primary side over the frequency. (c) Equivalent circuit of the transformer used to measure L_P. (d) Equivalent circuit of the transformer used to measure L_σ and R_W. (e) Saturation measurement results that confirm the specified saturation current of 1.5A.

TABLE V
EFFICIENCY COMPARISON BETWEEN CALCULATION, SIMULATION, AND MEASUREMENT OF THE *POWER SHEET* IN DC–DC OPERATION

		Calculation	Simulation	Measurement
V_{in} = 230 V, V_{out} = 20 V	P_{out}	38.0 W	38.0 W	38.0 W
	P_{in}	48.7 W	49.8 W	50.2 W
	P_{core}	6.5 W	6.6 W	
	P_{wind}	2.3 W	2.9 W	
	P_{res}	1.9 W	2.3 W	
	η_{tr}	80.1 %	80.0 %	
	η	78.1 %	76.3 %	75.2 %
V_{in} = 325 V, V_{out} = 20 V	P_{out}	76.3 W	76.1 W	76.3 W
	P_{in}	97.2 W	98.0 W	98.7 W
	P_{core}	9.4 W	9.7 W	
	P_{wind}	8.3 W	7.9 W	
	P_{res}	3.2 W	4.3 W	
	η_{tr}	81.2 %	81.2 %	
	η	78.5 %	77.6 %	77.3 %

primary resistance R_p (not R_W) is measured which fits very well to the calculation. The transformer configurations employed for the impedance measurements are indicated in Fig. 16(c) and (d). Fig. 16(e) illustrates the result of a saturation measurement; a current of $I_P = 1.5$ A can be applied to the flyback transformer without causing saturation which has been specified in the design procedure.

In order to verify the loss calculation and thus the calculated efficiency of the flyback transformer, η_{tr}, the *Power Sheet* is operated as a dc–dc converter at different input voltages V_{in}. Table V lists a comparison between the calculations, simulations, and measurements for $V_{in} = 230$ V and 325 V. The calculated losses are underestimated as the analytical model used

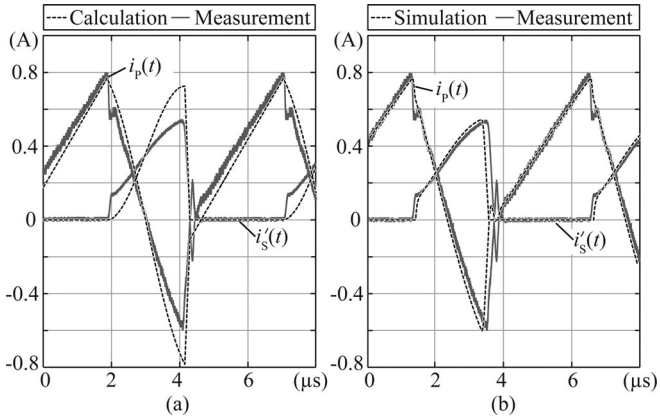

Fig. 17. (a) Comparison between calculated and measured transformer currents, i_P and i'_S. (b) Comparison between simulation and measurement of the transformer currents. The *Power Sheet* operates as dc–dc converter at $V_{in} = 230$ V, $V_{out} = 20$ V, and $P_{out} = 38$ W.

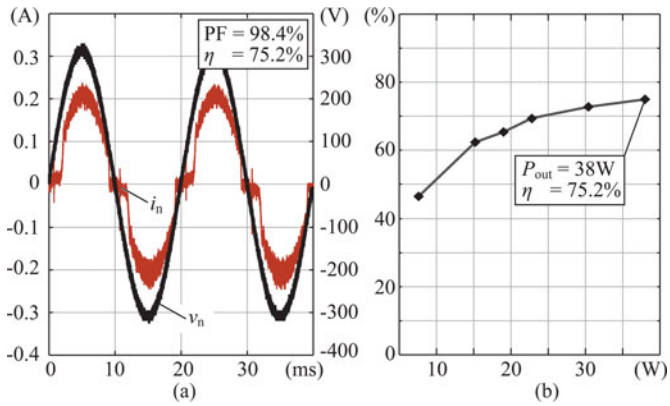

Fig. 18. (a) Input voltage v_n and input current i_n of the *Power Sheet* employing a PCB-integrated transformer ($V_{in} = 230$ V, $V_{out} = 20$ V, and $P_{out} = 38$ W). The input current is filtered employing an input inductor of $L = 460$ μH which is included in the efficiency measurement. (b) Efficiency η as a function of the output power P_{out}.

to calculate the voltage and current waveforms is considered to be lossless. Due to the rather low converter efficiency, however, a considerable energy is required to cover the losses from input to output, and this additional energy is not considered in the model. Fig. 17(a)shows a comparison between calculated and measured primary current i_P and secondary current i'_S (primary referred). The calculated currents consist of piecewise linear and sinusoidal waveforms, whereas the measurement currents are influenced by lossy and parasitic components in the converter. In order to consider these resistive and parasitic converter components, a simulation model implemented with Simplorer [41] is used in which the analytical core loss model according to Fig. 12(a) is still applied. Fig. 17(b) shows that the simulation waveforms fit well to the measured waveforms, and the estimated core and winding losses, P_{core} and P_{wind}, together with the calculated residual converter losses, P_{res} (semiconductor losses, snubber losses, gate drive losses), cover the measured converter losses [cf., Table V].

In PFC operation, the *Power Sheet* employing the designed PCB-integrated transformer achieves an efficiency of η =75.2%

and a power factor PF =98.4%. Fig. 18(a) shows the measurement result of the input voltage and the input current at nominal operation, and Fig. 18(b) depicts the efficiency η as a function of the output power $P_{\rm out}$. The rather low efficiency of the converter is the prize to be paid for the ultra-flat realization of the converter system.

V. Conclusion

For the realization of a 1-mm-thin PFC rectifier, the PCB integration of magnetic components is a key issue. This paper presents a multi-objective design procedure for ultra-flat magnetic components employing PCB-integrated cores which facilitates an optimized inductor or transformer design. Therefore, it is crucial to identify the magnetic material properly. Depending on the material and the shape of the core, anisotropic core losses, the need for isolation between the magnetic foils, or a proper reluctance model have to be considered in order to be able to meet a desired power loss per area limit and inductance value. All these issues are elaborated and shown by example on two amorphous materials (VITROVAC6155F and 2714A). The proposed design procedure considers different electrical, magnetic, and geometrical parameters in order to determine the component's configuration that is optimal with respect to minimum losses and/or minimum footprint area. The resulting Pareto Front is a vivid representation of the tradeoff, and different materials can easily be compared. The design procedure can be adapted for different core shapes or aspect ratios and is, therefore, a universal design tool for a PCB-integrated inductor or transformer. In order to verify the theoretical considerations, a prototype of a flyback transformer for a single-phase PFC rectifier ($V_{\rm in} = 230$ V, $V_{\rm out} = 20$ V, and $P_{\rm out} = 38$ W) has been built up. The shape of the transformer is beneficially for an anisotropic core material (VC6155F) as almost only the hard magnetization axis is utilized. This might differ for other core shapes. The achieved efficiency for the PFC rectifier is η =75.2%, which truly identifies a performance limit resulting from the extreme converter shape factor.

References

[1] D. Ge and Z. Chen, "On-chip boost DC-DC converter in color OLED driver & controller ICs for mobile application," in *Proc. 6th Int. Conf. ASIC*, 2005, vol. 1, pp. 459–463.

[2] J. Jacobs, D. Hente, and E. Waffenschmidt, "Drivers for OLEDs," in *Proc. Conf. Rec. 42nd IEEE Ind. Appl. Conf.*, Sep. 2007, pp. 1147–1152.

[3] J. Yoo, S. Jung, Y. Kim, S. Byun, J. Kim, N. Choi, S. Yoon, C. Kim, Y. Hwang, and I. Chung, "Highly flexible AM-OLED display with integrated gate driver using amorphous silicon TFT on ultrathin metal foil," *J. Display Technol.*, vol. 6, no. 11, pp. 565–570, 2010.

[4] D. G. Lamar, J. S. Zuniga, A. R. Alonso, M. R. Gonzalez, and M. M. Alvarez, "A very simple control strategy for power factor correctors driving high-brightness LEDs," *IEEE Trans. Power Electron.*, vol. 24, no. 8, pp. 2032–2042, Aug. 2009.

[5] S. Uchikoga, "Future trend of flat panel displays and comparison of its driving methods," in *Proc. IEEE Int. Symp. Power Semiconduct. Dev. IC's*, Jun. 2006, pp. 1–5.

[6] I. Josifovic, J. Popovic-Gerber, and J. Ferreira, "A PCB system integration concept for power electronics," in *Proc. 6th Int. IEEE Power Electron. Motion Control Conf.*, May 2009, pp. 756–762.

[7] C. Marxgut, J. Biela, and J. W. Kolar, "Design of a multi-cell, DCM PFC rectifier for a 1 mm thick, 200 W off-line power supply—The power sheet," presented at the 6th Int. Conf. Integr. Power Electron. Syst., Nuremberg, Germany, 2010.

[8] Infineon Technologies. (2012). [Online]. Available: http://www.infineon.com

[9] Murata Manufacturing Co., Ltd. (2012). [Online]. Available: http://www.murata.com

[10] R. Ulrich and L. Schaper, "Putting passives in their place," *IEEE Spectr.*, vol. 40, no. 7, pp. 26–30, Jul. 2003.

[11] Vishay. (2012). [Online]. Available: http://www.vishay.com

[12] Z. Ouyang, Z. Zhang, O. Thomsen, and M. Andersen, "Planar-integrated magnetics (PIM) module in hybrid bidirectional DC–DC converter for fuel cell application," *IEEE Trans. Power Electron.*, vol. 26, no. 11, pp. 3254–3264, Nov. 2011.

[13] EPCOS AG. (2012). [Online]. Available: http://www.epcos.com

[14] S. Orlandi, B. Allongue, G. Blanchot, S. Buso, F. Faccio, C. Fuentes, M. Kayal, S. Michelis, and G. Spiazzi, "Optimization of shielded PCB air-core toroids for high-efficiency DC-DC converters," *IEEE Trans. Power Electron.*, vol. 26, no. 7, pp. 1837–1846, Jul. 2011.

[15] E. Waffenschmidt, B. Ackermann, and J. A. Ferreira, "Design method and material technologies for passives in printed circuit board embedded circuits," *IEEE Trans. Power Electron.*, vol. 20, no. 3, pp. 576–584, May 2005.

[16] M. Ludwig, M. Duffy, T. O'Donnell, P. McCloskey, and S. OMathuna, "Design study for ultra-flat PCB-integrated inductors for low-power conversion applications," *IEEE Trans. Magnet.*, vol. 39, no. 5, pp. 3193–3195, Sep. 2003.

[17] C. O'Mathuna, N. Wang, S. Kulkarni, and S. Roy, "Review of integrated magnetics for power supply on chip (PwrSoC)," *IEEE Trans. Power Electron.*, vol. 27, no. 11, pp. 4799–4816, Nov. 2012.

[18] Q. Chen, Z. Gong, X. Yang, Z. Wang, and L. Zhang, "Design considerations for passive substrate with ferrite materials embedded in printed circuit board (PCB)," in *Proc. IEEE Power Electron. Special. Conf.*, Jun. 2007, pp. 1043–1047.

[19] Ferroxcube. (2012). [Online]. Available: http://www.ferroxcube.eu

[20] Y. Zhang and S. Sanders, "In-board magnetics processes," in *Proc. 30th Annu. IEEE Power Electron. Special. Conf.*, Aug. 1999, vol. 1, pp. 561–567.

[21] B. Bucheru and I. Jitaru, "ZVS and ZCS high efficiency low profile adapter," in *Proc. Power Convers. Intell. Motion Conf.*, Nuremberg, Germany, 2011, pp. 471–476.

[22] Schweizer Electronic AG. (2012). [Online]. Available:http://www.schweizer.ag

[23] Vacuumschmelze AG, VAC. (2012). [Online]. Available: http://www.vacuumschmelze.de

[24] Metglas. (2012). [Online]. Available: http://www.metglas.com

[25] TDK Corporation. (2012). [Online]. Available: http://www.tdk.com

[26] TOSHIBA. (2012). [Online]. Available: http://www.toshiba.com

[27] Hitachi Metals. (2012). [Online]. Available: http://www.hitachi-metals.co.jp

[28] C. Marxgut, J. Mühlethaler, F. Krismer, and J. W. Kolar, "Multi-objective optimization of ultra-flat magnetic components with a PCB-integrated core," in *Proc. IEEE 8th Int. Conf. Power Electron. ECCE Asia*, Jun. 2011, pp. 460–467.

[29] J. Mühlethaler, J. Biela, J. W. Kolar, and A. Ecklebe, "Improved core-loss calculation for magnetic components employed in power electronic systems," *IEEE Trans. Power Electron.*, vol. 27, no. 2, pp. 964–973, Feb. 2012.

[30] J. Mühlethaler, J. Biela, J. W. Kolar, and A. Ecklebe, "Core losses under the DC bias condition based on Steinmetz parameters," *IEEE Trans. Power Electron.*, vol. 27, no. 2, pp. 953–963, Feb. 2012.

[31] L. Coppola, D. Cottet, and F. Wildner, "Investigation on current density limits in power printed circuit boards," in *Proc. 23rd Annu. IEEE Appl. Power Electron. Conf. Expo.*, Feb. 2008, pp. 205–210.

[32] J. Mühlethaler, J. Kolar, and A. Ecklebe, "A novel approach for 3D air gap reluctance calculations," in *Proc. 8th Int. Conf. Power Electron.*, May/Jun. 2011, pp. 446–452.

[33] R. Prieto, J. Cobos, O. Garcia, P. Alou, and J. Uceda, "Study of 3-D magnetic components by means of "double 2-D" methodology," *IEEE Trans. Ind. Electron.*, vol. 50, no. 1, pp. 183–192, Feb. 2003.

[34] E. Snelling, *Soft Ferrites—Properties and Applications*, 2nd ed. Mendham, NJ: PSMA, 2005.

[35] J. Qiu and C. Sullivan, "Design and fabrication of VHF tapped power inductors using nanogranular magnetic films," *IEEE Trans. Power Electron.*, vol. 27, no. 12, pp. 4965–4975, Dec. 2012.

[36] P. Dowell, "Effects of eddy currents in transformer windings," *Electr. Eng. Proc. Inst.*, vol. 113, no. 8, pp. 1387–1394, 1966.
[37] I. Lope, C. Carretero, J. Acero, J. Burido, and R. Alonso, "Practical issues when calculating ac losses for magnetic devices in PCB implementations," in *Proc. 27th Annu. IEEE Appl. Power Electron. Conf. Expo.*, Feb. 2012, pp. 1017–1022.
[38] G. Spiazzi, L. Rossetto, and P. Mattavelli, "Design optimization of soft-switched insulated DC/DC converters with active voltage clamp," in *Proc. Conf. Rec. 31st IEEE Ind. Appl. Conf.*, Oct. 1996, vol. 2, pp. 1169–1176.
[39] Y. Hsieh, M. Chen, and H. Cheng, "An interleaved flyback converter featured with zero-voltage transition," *IEEE Trans. Power Electron.*, vol. 26, no. 1, pp. 79–84, Jan. 2011.
[40] A. Emrani, E. Adib, and H. Farzanehfard, "Single-switch soft-switched isolated DC-DC converter," *IEEE Trans. Power Electron.*, vol. 27, no. 4, pp. 1952–1957, Apr. 2012.
[41] ANSYS, Inc. (2012). [Online]. Available: http://www.ansys.com

Christoph Marxgut (S'09) studied electrical engineering at the University of Technology Vienna, Austria, focusing on control systems and measurement technology. He received the Dipl.-Ing. (M.Sc.) degree (with Hons.) from the University of Technology, Vienna, in October 2008. Since November 2008, he has been working toward the Ph.D. degree with the Power Electronic Systems Laboratory, Swiss Federal Institute of Technology Zurich (ETH Zurich), Zurich, Switzerland.

During his studies, he delved into energy technology and power systems at the ETH Zurich. In his Master Thesis, which he wrote at the ETH Zurich, he worked on modulator design for pulsed power systems.

Jonas Mühlethaler (S'09) received the M.Sc. and Ph.D. degrees in electrical engineering from the Swiss Federal Institute of Technology Zurich (ETHZ), Zurich, Switzerland, in 2008 and 2012, respectively.

His master studies was focused on power electronics and electrical machines. In his M.Sc. thesis, which he wrote at ABB Corporate Research in Sweden, he worked on compensating torque pulsation in permanent magnet motors. In 2008 he joined the Power Electronic Systems Laboratory (PES), ETHZ, to work toward the Ph.D. degree. During the Ph.D. studies, he worked on modeling and multi-objective optimization of inductive power components. He is currently a Postdoctoral Fellow at PES.

Florian Krismer (S'05–M'12) received the M.Sc. degree (with Hons.) from the University of Technology Vienna, Vienna, Austria, in 2004, and the Ph.D. degree from the Power Electronic Systems Laboratory (PES), Swiss Federal Institute of Technology (ETH) Zürich, Zürich, Switzerland, in 2011.

His research interests include the analysis, design, and optimization of high-current and high-frequency power converters. He is currently a Postdoctoral Fellow with PES, ETH Zürich.

Johann W. Kolar (S'89–M'91–SM'04–F'10) received the M.Sc. and Ph.D. degrees (*summa cum laude/promotio sub auspiciis praesidentis rei publicae*) from the Vienna University of Technology, Vienna, Austria.

Since 1984, he has been an Independent International Consultant in close collaboration with the Vienna University of Technology, in the field of power electronics, industrial electronics, and high-performance drives. He has proposed numerous novel converter topologies and modulation/control concepts, e.g., the VIENNA Rectifier, the Swiss Rectifier, and the three-phase ac–ac sparse matrix converter. He has published more than 450 scientific papers in international journals and conference proceedings and has filed more than 85 patents. He became a Professor and Head of the Power Electronic Systems Laboratory, Swiss Federal Institute of Technology (ETH) Zurich, Zurich, Switzerland, on February 1, 2001. The focus of his current research is on ac–ac and ac–dc converter topologies with low effects on the mains, e.g., for data centers, more-electric-aircraft and distributed renewable energy systems, and on solid-state transformers for smart microgrid systems. Further main research areas are the realization of ultracompact and ultraefficient converter modules employing latest power semiconductor technology (SiC and GaN), micropower electronics and/or power supplies on chip, multidomain/scale modeling/simulation and multi-objective optimization, physical model-based lifetime prediction, pulsed power, and ultra high speed and bearingless motors.

Dr. Kolar has been appointed an IEEE Distinguished Lecturer by the IEEE Power Electronics Society (PELS) in 2011. He received an IEEE Transactions Prize Paper Award of the IEEE Industrial Electronics Society in 2005, of the IEEE Industrial Applications Society (IAS) in 2009 and 2010, the IEEE/ASME in 2010, and of the IEEE PELS in 2009, 2010, and 2011. He also received the Best Paper Award at the International Conference on Performance Engineering 2007, the IAS 2008, the IECON 2009, the International Symposium on Parameterized and Exact Computation 2010 (for two papers), the ECCE Energy Conversion Congress and Exposition (ECCE) Asia 2011, and the ECCE USA 2011. Furthermore, he received the ETH Zurich Golden Owl Award 2011 for Excellence in Teaching and an Erskine Fellowship from the University of Canterbury, New Zealand, in 2003. He initiated and/or is the founder/cofounder of four spin-off companies targeting ultra high speed drives, multidomain/level simulation, ultracompact/efficient converter systems, and pulsed power/electronic energy processing. In 2006, the European Power Supplies Manufacturers Association awarded the Power Electronics Systems Laboratory of ETH Zurich as the Leading Academic Research Institution in Power Electronics in Europe. He is a Member of the IEEJ and of International Steering Committees and Technical Program Committees of numerous international conferences in the field (e.g., the Director of the Power Quality Branch of the International Conference on Power Conversion and Intelligent Motion). He is the founding Chairman of the IEEE PELS Austria and Switzerland Chapter and Chairman of the Education Chapter of the EPE Association. From 1997 to 2000, he served as an Associate Editor of the IEEE TRANSACTIONS ON INDUSTRIAL ELECTRONICS, and since 2001, has been an Associate Editor of the IEEE TRANSACTIONS ON POWER ELECTRONICS. Since 2002, he has also been an Associate Editor of the *Journal of Power Electronics* of the Korean Institute of Power Electronics and a member of the Editorial Advisory Board of the *IEEJ Transactions on Electrical and Electronic Engineering*.